
Article:
Wilby, A. orcid.org/0009-0005-0731-0997, Corteen, J., Lewis, S. et al. (2 more authors) (2023) Nano and micro-indentation driven characterisation of asperity and bulk plasticity at the surface of modern premium rail steels. Wear. 205004. ISSN 0043-1648

https://doi.org/10.1016/j.wear.2023.205004

Wear 530–531 (2023) 205004

Contents lists available at ScienceDirect

Wear

journal homepage: www.elsevier.com/locate/wear

Nano and micro-indentation driven characterisation of asperity and bulk plasticity at the surface of modern premium rail steels

A. Wilby [a,*], J. Corteen [b], S. Lewis [b], R. Lewis [a], D.I. Fletcher [a]

[a] Department of Mechanical Engineering, University of Sheffield, Mappin Street, Sheffield, S1 3JD, UK
[b] British Steel, Brigg Road, Scunthorpe, Lincolnshire, DN16 1XA, UK

ARTICLE INFO

Keywords:
Rail steel
Plastic deformation
Microstructural analysis
Material property data
Strain accumulation modelling
Twin-disc testing

ABSTRACT

The plastic deformation behaviour of rail steels due to cyclic rail-wheel contacts is important to understand due to its connection to wear and rolling contact fatigue (RCF) damage initiation in service. Simulation models such as the 'Layer' and 'Brick' model have previously been developed to estimate the accumulation of plastic damage in a rail steel; however, the data available to drive these models is currently sparse, with limited applicability to modern rail steel grades. This paper presents the research examining the shear stress-strain curve relationships of rail steels derived from plastic shear strain and shear yield stress data collected from twin-disc test samples. A combination of microhardness and nanohardness testing was used to derive the shear yield stress data, whereas the plastic shear strain was acquired from optical microscopy. Six different conditions were investigated for this research for the purpose of examining how shear stress-strain curve relationships compared between the standard R260 and the premium HP335 and R350HT rail steels and how this compares to wear damage data. The influence of the maximum Hertzian contact pressure on the shear stress-strain curve relationships of R260 between 600 and 1500 MPa contact pressure was also investigated. The wear rate results derived from the mass loss in interrupted twin-disc tests showed HP335 wearing the least, followed by R350HT and then R260 for 1500 MPa, dry contact conditions. However, the highest shear yield stress achieved was for R350HT, then HP335, and R260. The results show that the shear stress-strain curve relationships by themselves are insufficient to determine rail steel wear performance in a laboratory environment. The shear stress-strain curve relationships for R260 collected under different contact pressures showed the results are near independent of the contact pressure within the range explored.

Author statement

Adam Wilby: Investigation, Methodology, Conceptualisation, Formal Analysis, Writing – Original Draft **David Fletcher:** Conceptualisation, Supervision, Writing – review and editing, Funding acquisition **Jacob Corteen:** Conceptualisation, Supervision, Resources, Writing – review and editing **Roger Lewis:** Supervision, Writing – review and editing **Steve Lewis:** Conceptualisation, Writing – review and editing.

1. Introduction

Rail steels in-service are typically subjected to a combination of high compression and high shear stress that produces large amounts of plastic deformation localised on the surface of the rail head. This plastic deformation is known to be the cause of significant incidences of wear and rolling contact fatigue (RCF) damage mechanisms in rail [1]. These two damage mechanisms are undesirable as they affect the safe running of rail networks and lead to the undertaking of expensive track maintenance programmes (grinding/milling/weld repair/replacement) to remove them or their effects. For example, during the 2020/21 financial year the cumulative track renewal expenditure by Network Rail in the UK was £1,207 m [2]. An improved quantification of the rail steel response to load can, therefore, allow the selection of rail steel grades to be better targeted to the duty they will experience in track. In addition, it can provide the opportunity for track maintenance programmes to be optimised.

The near surface deformation in rail steels is typically dominated by a plastic ratchetting loading response. The ratcheting theory describes this loading response as the incremental accumulation of shear strain in

* Corresponding author.
E-mail address: awilby1@sheffield.ac.uk (A. Wilby).

https://doi.org/10.1016/j.wear.2023.205004
Received 27 February 2023; Received in revised form 5 May 2023; Accepted 3 June 2023
Available online 3 June 2023

Table 1
Overview of the different twin-disc test conditions investigated.

Condition	Rail Steel Grade	Wheel Steel Grade	Maximum Contact Pressure (MPa)	Percentage Creep (%)	Nominal Speed	Total Number of Contact Cycles for the Rail Sample
1	R260	R8T	1500	−1	400	80000 in 10000 increments (3), 500 (2), 15000 (2), 40000 (2), 70000 (2)
2	HP335	R8T	1500	−1	400	80000 in 10000 increments (3), 15000, 40000, 70000
3	R350HT	R8T	1500	−1	400	80000 in 10000 increments (3), 15000, 40000, 70000
4	R260	R8T	1200	−1	400	80000 in 10000 increments, 15000, 40000, 70000
5	R260	R8T	900	−1	400	120000 in 10000 increments, 15000, 40000, 70000
6	R260	R8T	600	−1	400	120000 in 10000 increments, 15000, 40000, 70000

Table 2
Chemical composition of the rail and wheel steels tested according to the specification [29–31].

Material	Chemical Composition (wt%)										
	C	Si	Mn	P	S	Cr	Al	Cu	Mo	Ni	V
R260	0.62–0.80	0.15–0.58	0.70–1.20	≤0.025	≤0.025	≤0.15	≤0.004	≤0.15	≤0.02	≤0.10	≤0.03
HP335	0.87–0.97	0.75–1.00	0.75–1.00	≤0.020	0.008–0.020	≤0.10	≤0.004	–	–	–	0.09–0.13
R350HT	0.70–0.82	0.13–0.60	0.65–1.25	≤0.025	≤0.030	≤0.15	≤0.004	≤0.15	≤0.02	≤0.10	≤0.03
R8T	≤0.56	≤0.40	≤0.80	≤0.040	≤0.040	≤0.30	–	≤0.30	≤0.08	≤0.30	≤0.05

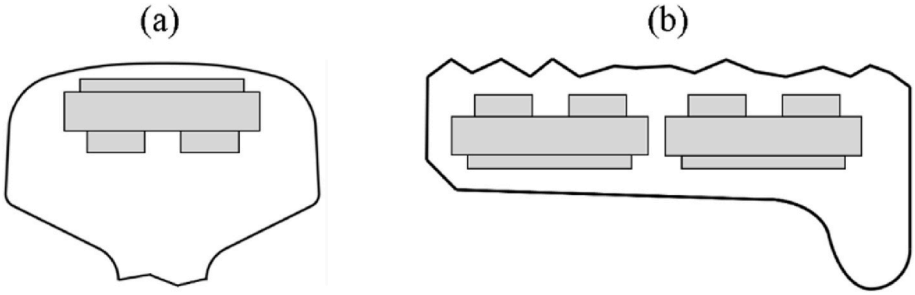

Fig. 1. Illustration of the orientation the (a) rail and (b) wheel twin-disc samples were machined out of a full-sized rail and railway wheel with the specimen running track prepared to an average surface roughness of 0.5 μm.

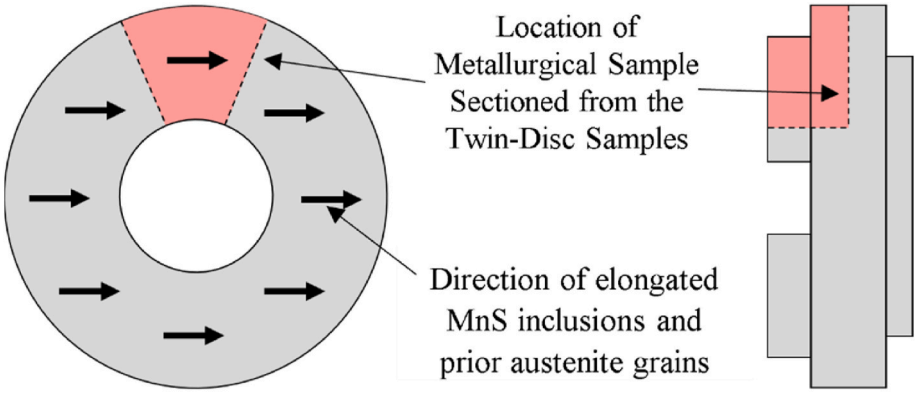

Fig. 2. Illustration showing how the metallurgical specimens were sectioned from the twin-disc samples in relation to the orientation of the elongated MnS inclusions.

the rail steel material with every contact cycle when the rail-wheel contact stresses are above the rail steel's plastic shakedown limit [3]. The 'Layer' [4] and 'Brick' [5] models are two simulation models developed based on the principle of plastic ratchetting to enable the strain accumulation in rail steels to be predicted. The shear stress-strain curve relationship, alongside the ratcheting load conversion factor (conversion factor between the ratcheting load experienced by a material and the plastic shear strain accumulated), and the critical shear strain to failure are the data inputs needed to run these models. The loading conditions of combined compression and shear mean that deriving the shear stress-strain curve relationship via tensile tests is insufficient to describe the loading response in-service due to the inability to reach the extremely high shear strains which can be observed in some rails removed from service. Alternative methods of deriving the shear stress-strain curve relationship for rail steels from twin-disc tests have been developed [4,6]. This initial method has subsequently been modified simultaneously by Tomlinson et al. [7] and Alwahdi et al. [8] to improve data acquisition efficiency to enable this data to be derived from a single twin-disc sample or used rail section.

The more efficient generation of data for these models can enable the

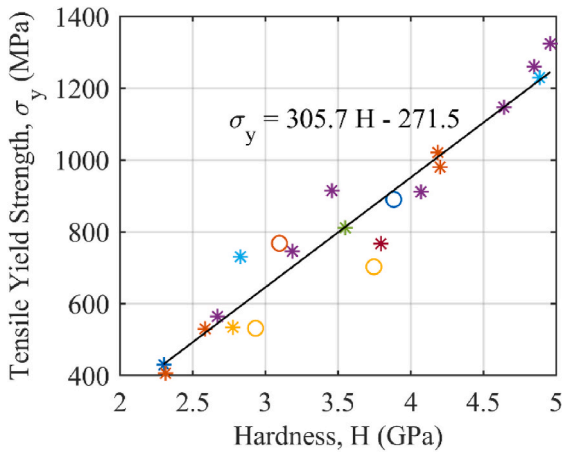

Fig. 3. Hardness against tensile yield strength relationship derived for various rail steels of different metallurgies and microstructures (pearlite, bainitic, heat-treated). The different colour and style of marker denotes a different source the data was obtained from. (For interpretation of the references to colour in this figure legend, the reader is referred to the Web version of this article.)

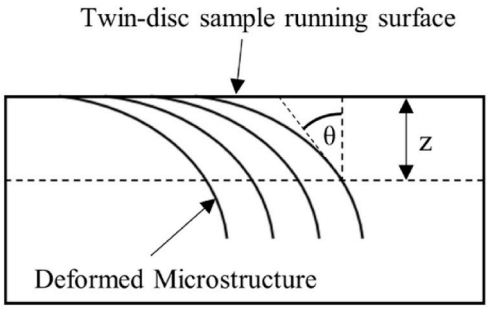

Fig. 4. Illustration to show how the angle of the deformed microstructure is measured from the optical micrographs.

opportunity to answer additional questions regarding potential behaviour change of rail steels subjected to different contact conditions. The current rail steel data obtained to characterise their plasticity response have mainly been derived for 1500 MPa, 1% slip, dry contact conditions [6,7,9], with limited data collected outside of these parameters. It is, therefore, currently unknown whether the data generated under these conditions should be regarded as 'material property' data or whether it is 'system behaviour' data only relevant to a limited range of service conditions.

This paper presents part of a larger body of work developing improvements to data collection in characterising the plastic deformation response of rail steels using twin-disc tests. Data is generated for harder, premium, rail steels that have not previously been characterised. A range of contact pressures is used to reveal whether the information collected is 'material property' or 'system behaviour' data.

2. Experimental procedure

To replicate the accumulation of plastic shear strain in rail steels twin-disc tests were performed using the Sheffield University ROlling Sliding (SUROS2) twin-disc machine. SUROS2 [10] is a modified TE72 twin-disc machine [11] operating on identical principles to the original SUROS twin-disc machine. This accepts the same 47 mm diameter 10 mm wide running track sample design as the earlier machine which has generated significant volumes of the existing data on rail steel plastic response [12].

A summary of the twin-disc tests conducted in this investigation is shown in Table 1. The six different conditions investigated enabled two sets of comparisons to be conducted. Conditions 1, 2, and 3 enable a comparison of the plastic deformation behaviour of the premium rail steels grades HP335 and R350HT against the standard rail steel grade R260. Conditions 1, 4, 5, and 6 were conducted to understand how changing the maximum Hertzian contact pressure may influence the plastic deformation response of the rail steel R260. The chemical composition of the different rail steel grades and the R8T wheel steel used for this investigation are provided in Table 2. Tests interrupted every 10,000 contact cycles were used to understand the rail steel wear behaviour for each condition and hence identify when a steady-state regime is achieved. The uninterrupted tests were performed to collect data characterising the plastic damage observed after different contact cycle durations. The data collected from the uninterrupted tests, provide the basis for raw information to derive the shear stress-strain curve relationship, ratcheting load conversion factor, and critical shear strain to failure for each condition that can be used in ratcheting models [4]. The experiments performed across closely spaced increments of contact cycle duration for each condition examined, so although no repeat tests under identical conditions were performed any anomalies in the experiments would have been identified.

To ensure the sample metallurgies examined were representative of actual rail and wheel steel, the twin-disc samples were machined out of a full-scale railhead and railway wheel tread, as illustrated in Fig. 1. The running track of the twin-disc samples was ground to an average surface roughness Ra less than 0.5 μm. Prior to testing, both the rail and wheel twin-disc samples were cleaned in an ultrasonic bath with acetone. In addition, the mass, running track width, and running track diameter of the twin-disc samples was measured at the start, during each interruption, and at the end of each experiment conducted. A thermometer and hygrometer were used to record the temperature and relative humidity conditions of the SUROS2 laboratory at the start of each experiment recording an average of 19.4 °C and 47% across the experiments. The standard deviation observed with these readings was 2.5 °C and 7%, respectively. Traction coefficient data is particularly sensitive to environmental conditions, but no outliers were observed to suggest the tests were significantly influenced by the laboratory environment. To observe the plastic deformation following testing samples were sectioned to reveal the circumferential plane halfway across the running track as shown in Fig. 2. The metallurgical samples were taken from the portion of the discs where the elongated MnS inclusions were orientated parallel to the running track to ensure the data collected was representative of the correct orientation of the rail steel microstructure that is plastically deformed in full-scale rail-wheel contacts. This orientation of these inclusions present in the microstructure of all three rail steel metallurgies examined provide an indication of the rail sections longitudinal direction resulting from the hot rolled manufacturing process. The sectioned metallurgical samples were then mounted in Bakelite, ground using SiC paper to P1200 grit, followed by polishing using diamond and alumina suspension down to a 0.05 μm surface finished. A 2% Nital etching solution was used to reveal the rail steels microstructural plastic damage for optical microscopy.

Both microhardness and nanohardness testing were undertaken to characterise the near surface hardness in the polished metallurgical samples. The microhardness testing was used to measure the hardness vs. depth in the bulk of the material, whereas nanohardness testing was conducted near the running track surface. The microhardness tests were done using a Struers Duramin-40 microhardness indenter with an array of indents performed at a minimum depth of 60 μm up to 1.5 mm below the running surface in 20 μm increments. A 50 g indentation load with a 15 s dwell time was used to collect this data to allow the indents to be as small as feasibly possible to minimise the required indent separation distance, while still being large enough to measure. To comply with the spacing requirements in the British Standard BS EN 6507–1:2018 [13], the indent array was staggered into three columns with a column separation of 100 μm.

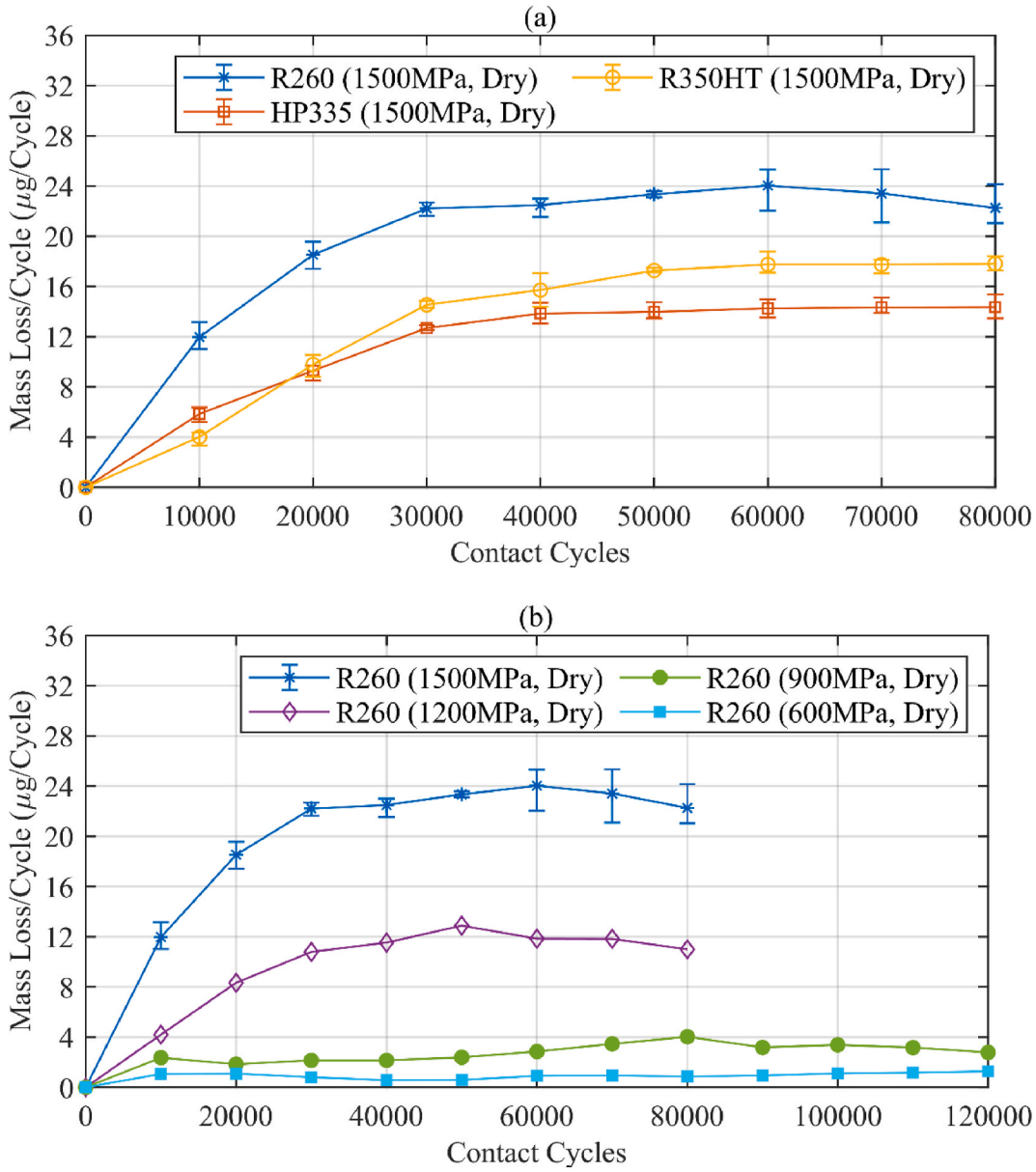

Fig. 5. Mass loss per cycle against contact cycles results. (a) Hardness results obtained for study 1 comparing the three different rail steels R260, HP335, and R350HT at 1500 MPa, 1% slip, dry contact conditions. (b) Hardness results obtained for study 2 comparing the effect of four different maximum contact pressure 1500 MPa, 1200 MPa, 900 MPa, and 600 MPa for R260 rail steel subjected to 1% slip, dry contact conditions.

The nanohardness tests were conducted using a Bruker Hysitron TS 77 Select nanohardness indenter utilising the mechanical property mapping feature. The mechanical property maps consisted of a 10 × 10 grid of nano indents equally separated by 3 μm with each indent taken using a standard Berkovich diamond tip with an indentation load of 2 mN. Nanohardness values were derived from the indenter properties and load against displacement curves using the Oliver and Pharr method [14]. For each metallurgical sample two datasets were collected: i) a plastic deformation region dataset consisting of a 4 × 10 grid of mechanical property maps equally separated by 30 μm, with the grid's long axis orientated perpendicular to the running surface. ii) An undeformed region dataset for reference against bulk properties, consisting of a 5 × 8 grid of mechanical property maps equally separated by 100 μm located at a minimum depth of 2 mm below the twin-disc samples running surface. The depth of the nano indentations relative to the twin-disc samples running surface was measured from optical micrographs.

A measure of the average undeformed hardness for the three rail steel grades investigated was also collected during microhardness testing. For this data, ten 10 kg indentation load indents with a 15 s dwell time were performed on each rail steel grade. The location of these indents was in the undeformed substrate far away from any observable plastic damage.

3. Shear stress-strain curve relationship derivation procedure

The shear stress-strain curve relationships were derived from a single twin-disc sample experiencing steady-state conditions using the same methodology simultaneously developed by Tomlinson et al. [7] and Alwahdi et al. [8]. In this method, shear strain and shear stress data were collected in parallel and then combined to obtain the shear stress-strain curve. A modified Voce equation, in the form of Equation (1), was then fitted to the data points to derive a numerical expression of the shear stress-strain curve relationship.

$$\tau = m\left(1 - e^{-n(\gamma)}\right)^{p} \qquad \text{Equation 1}$$

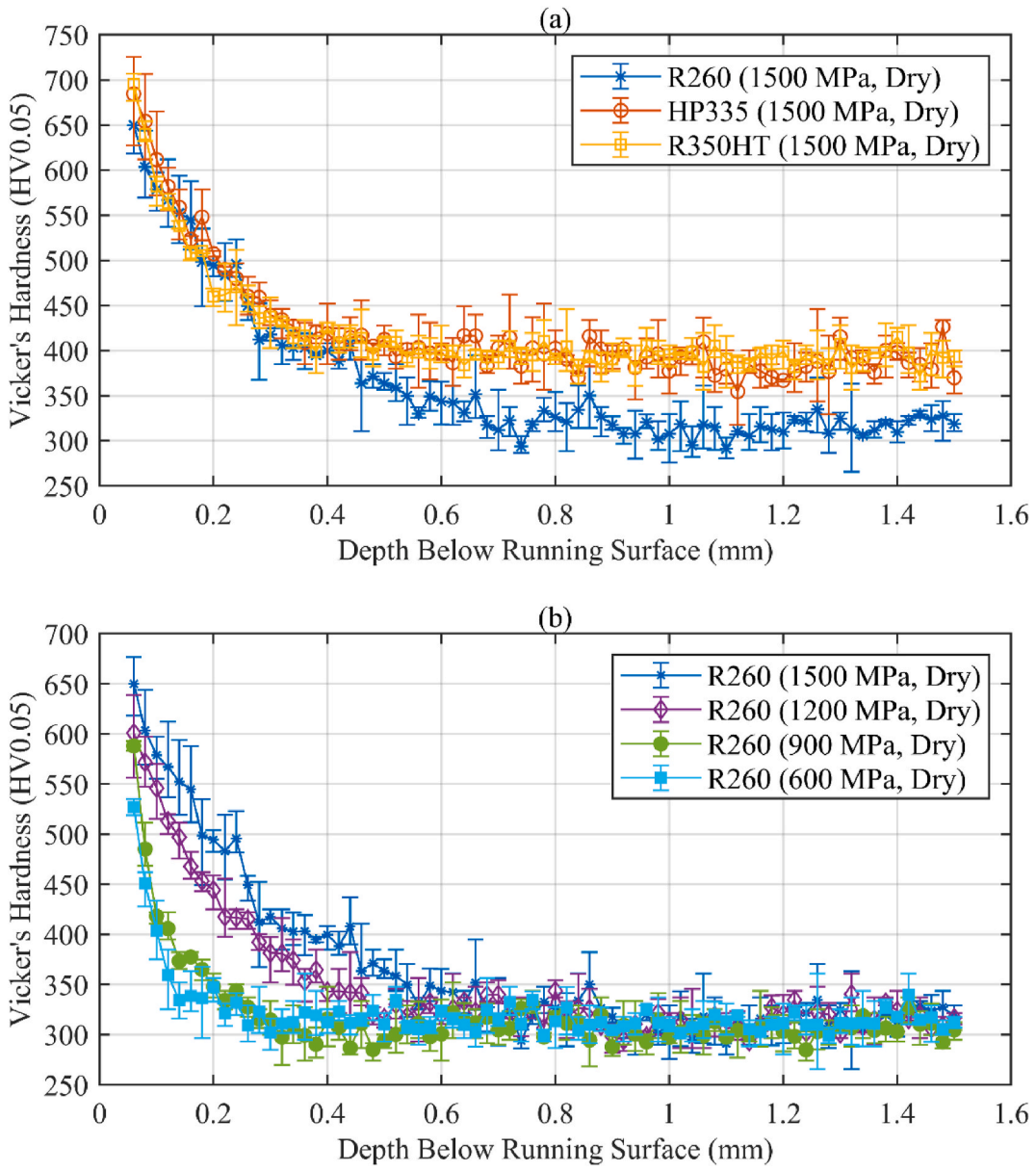

Fig. 6. Comparison of the microhardness against depth results obtained from the twin-disc samples tested up to 70,000 contact cycles for a) R260 (1500 MPa), HP335 (1500 MPa), and R350HT (1500 MPa); and b) R260 (1500 MPa, 1200 MPa, 900 MPa, 600 MPa) under dry contact conditions.

where *m, n, p* are coefficients of the modified Voce equation found by fitting the relationship to the experimental shear stress-strain curve data points.

3.1. Shear stress data component

The shear stress data was derived from the microhardness and nanohardness measurements characterising the subsurface hardness variation with depth beneath the twin-disc samples running surface. As different indentation loads were used to collect the microhardness and nanohardness data, the two hardness datasets were combined by normalising the results in terms of percentage work hardening based on their respective hardness measurement of the rail steels undeformed substrate. This normalisation process avoids issues with the indentation size effect that prevents direct comparison of the magnitude of the hardness measurements using different indentation loads. This manifests itself through an observed increased in hardness with decreasing indentation size, where the increased hardening occurs due to geometrical necessary dislocations being generated from the large strain gradients in small indentations [15]. After normalising the data an expression in the form of Equation (2) was then fitted to the data to derive relationships of the percentage work hardening against depth. A weighting was applied to the microhardness results in proportion to the volume of microhardness data compared to the nanohardness data collected.

$$\frac{H}{H_0} = A\exp(Bx) + C\exp(Dx) + 100 \qquad \text{Equation 2}$$

where, *A, B, C, D* are coefficients found by fitting the expression to the percentage work hardening data. The two exponential terms in the expression allow fitting to both the bulk and asperity contact driven contributions to the plastic damage. These relationships were subsequently converted to shear stress utilising the assumption that the increase in the percentage work hardening is proportional to the percentage increase in shear strength as given by Equation (3).

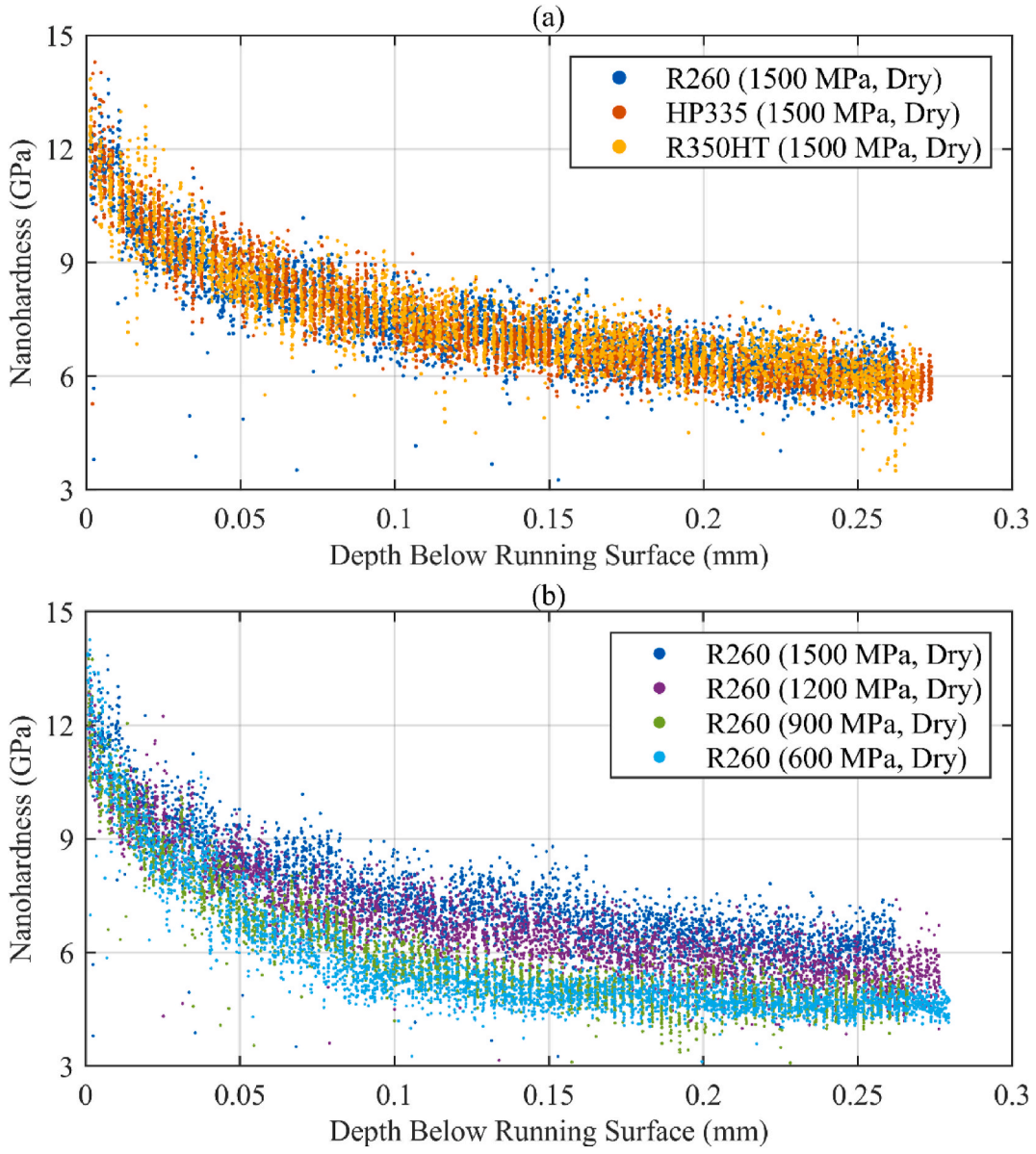

Fig. 7. Comparison of the nanohardness against depth results obtained from the twin-disc samples tested up to 70,000 contact cycles for a) R260 (1500 MPa), HP335 (1500 MPa), and R350HT (1500 MPa); and b) R260 (1500 MPa, 1200 MPa, 900 MPa, 600 MPa) under dry contact conditions.

$$k = k_0\left(\frac{H}{H_0}\right) \quad \text{Equation 3}$$

where k_0 is the rail steels initial shear yield strength. The initial shear yield strength of each rail steel was determined by converting the average bulk hardness obtained from the 10 kg indentation load microhardness results using a hardness against tensile yield strength relationship derived for rail steels, Fig. 3. The data used to create this relationship were obtained from hardness and tensile test results in academic literature [9,16–26] and from internal tests conducted within British Steel [27]. Due to the hardness results collected from literature being generated under different indentation loads, the hardness data were normalised to correct the indentation size effect and to become based on a 10 kg indentation load. An understanding of the indentation size effect error with indentation load was characterised by measuring the apparent Vickers hardness reported by the Duramin-40 microhardness indenter for R260 for indentation loads ranging from 0.01 to 10 kg. The tensile yield strength σ_0 was then converted to a shear yield strength using Tresca's yield criterion, as given in Equation (4).

$$k_0 = \frac{\sigma_0}{2} \quad \text{Equation 4}$$

3.2. Shear strain data component

The shear strain data were derived from the plastic damage observed in the captured optical micrographs of the etched metallurgical samples. Shear strain was obtained by measuring the angle θ of the observed deformed microstructure relative to the normal of the twin-disc samples running surface at different depths z below the running surface as shown in Fig. 4. These angles were then converted to shear strain using Equation (5).

$$\gamma = \tan(\theta) \quad \text{Equation 5}$$

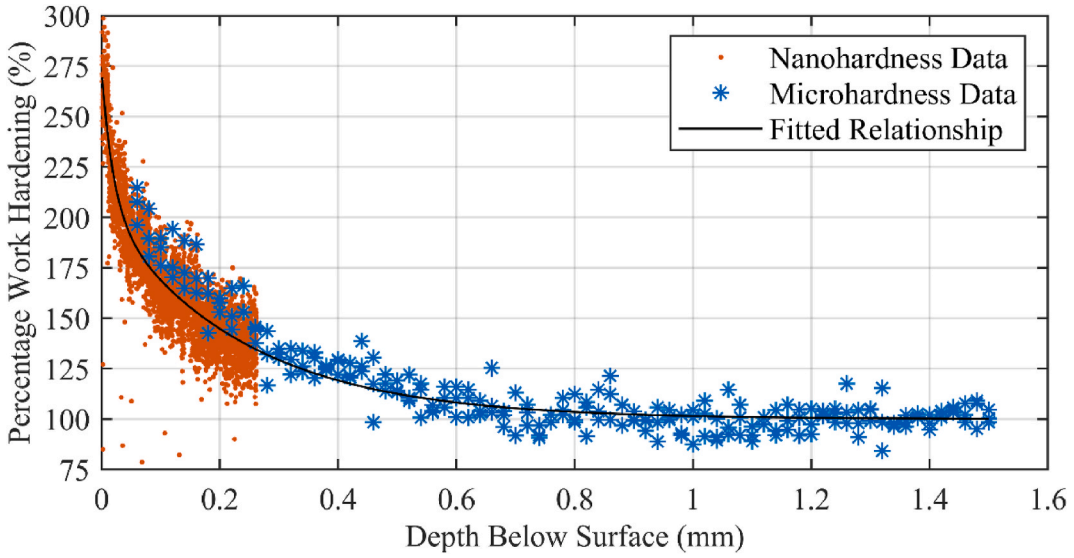

Fig. 8. Example showing the percentage work hardening against depth relationships derived from the combined microhardness and nanohardness data.

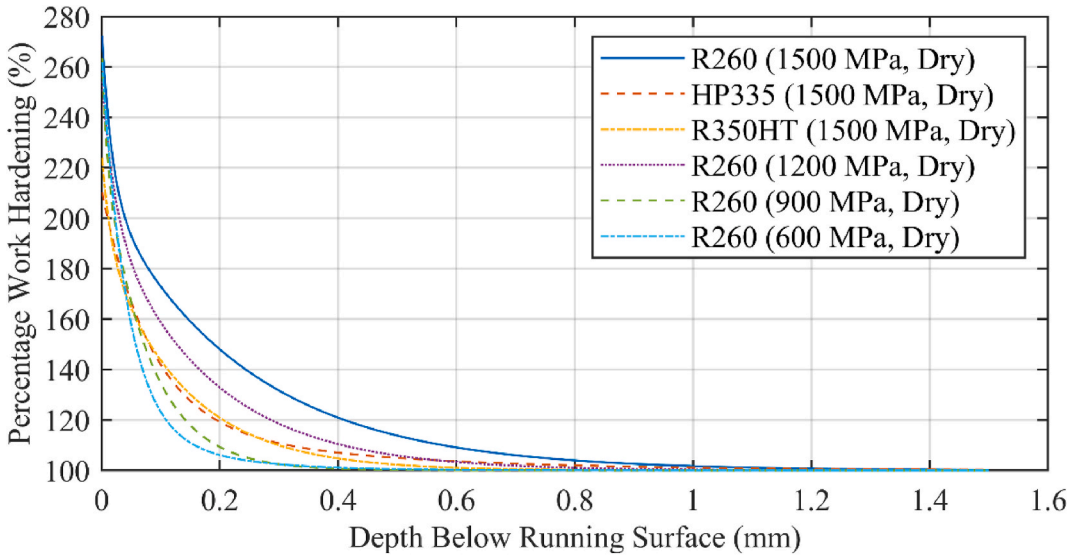

Fig. 9. Percentage work hardening against depth relationships derived for R260 (1500 MPa, 1200 MPa, 900 MPa, 600 MPa), HP335 (1500 MPa), and R350HT (1500 MPa) under dry contact conditions.

4. Results

4.1. Wear rate results

The evolution of the rail steel wear rate with contact cycles calculated from the interrupted twin-disc test mass change results are presented in Fig. 5a-b. In Fig. 5a comparing the wear rate evolution for the three different rail steel metallurgies (R260, HP335, R350HT) at the same 1500 MPa, dry contact conditions a clear ranking can be observed once steady-state conditions were achieved. The results showed HP335 wearing the least (14.15 μg/cycle), followed by R350HT (17.65 μg/cycle) and then R260 (22.96 μg/cycle). The steady-state wear conditions were achieved by the rail steels R260, HP335, and R350HT at 30,000, 40,000, and 50,000 contact cycles, respectively. This point was defined using approach of Tyfour et al. [9] to identify the number of contact cycles at which there is a distinct reduction in the wear rate after which variation is of the order of the experimental uncertainty.

In Fig. 5b, comparing the wear rates of R260 across different maximum Hertzian contact pressures, wear rates decreased with decreasing contact pressure. The tests conducted with 1500 MPa and 1200 MPa contact pressure show steady-state wear conditions being achieved by 30,000 and 40,000 contact cycles, respectively. For the tests conducted at 900 MPa and 600 MPa a different wear rate behaviour was observed with wear rates staying relatively constant throughout the tests.

4.2. Hardness results

A comparison of the microhardness against depth results obtained from the twin-disc samples tested up to 70,000 contact cycles for all six conditions investigated, are shown in Fig. 6a-b. In Fig. 6a, comparing the three rail steel grades under 1500 MPa, dry contact conditions, R260 presented the microhardness increase up to a depth of approximately 700 μm. In contrast, HP335 and R350HT exhibited roughly identical depths of microhardness increase, to about 400 μm. For depths less than 400 μm the microhardness against depth results for all three rail steel grades were roughly identical and followed the exact same trend, even though the rail steels investigated have different baseline undeformed

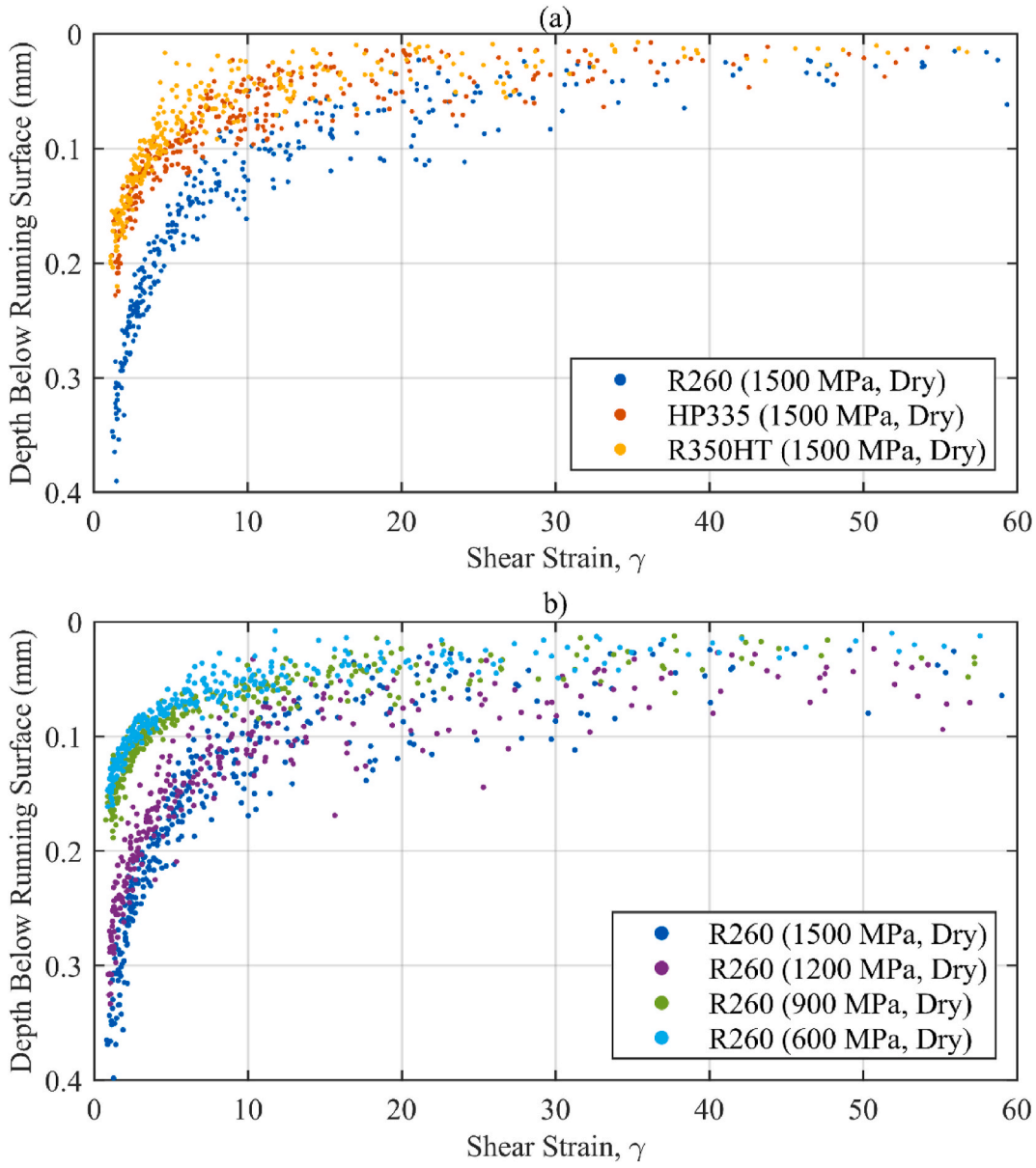

Fig. 10. Comparison of the shear strain against depth results obtained from the twin-disc samples tested up to 70,000 contact cycles for a) R260 (1500 MPa), HP335 (1500 MPa), and R350HT (1500 MPa); and b) R260 (1500 MPa, 1200 MPa, 900 MPa, 600 MPa) under dry contact conditions.

Table 3
Shear yield strength results of R260, HP335, and R350HT rail steel.

Rail Steel Grade	Hardness (HV10.0)	Tensile Yield Strength (MPa)	Shear Yield Strength (MPa)
R260	285	583	292
HP335	340	748	374
R350HT	350	779	390

hardness.

In Fig. 6b comparing R260 under different contact pressures for dry contact conditions, the depth of hardness increase is reduced for the experiments conducted with lower maximum contact pressures. The depth of raised hardness decreased from 700 μm at 1500 MPa, to 500 μm at 1200 MPa, and 250 μm at 900 MPa. There was only a marginal change in the depth of increased hardness between the R260 steel tested at 900 and 600 MPa contact pressure.

Fig. 7a-b shows the nanohardness against depth results obtained from the twin-disc samples tested up to 70,000 contact cycles for all six conditions investigated. For all six conditions examined the rail steels achieved roughly identical values of hardness of about 12 GPa at the running surface. In addition, for data collected at very shallow depths of less than about 50–100 μm there is a noticeable uptick in the nanohardness against depth results compared to the data collected at much greater depths below the running surface.

Fig. 8 shows an example of how the normalised microhardness and nanohardness against depth results were combined to find the percentage work hardening relationships for R260 subject to 1500 MPa, dry contact conditions. As can be seen, the normalised microhardness data presented the same hardness against depth trend compared to the normalised nanohardness data but offset about 30 μm deeper below the running surface. The reason for this offset was thought to be due to the different indent size between the techniques. The larger size of microhardness indents means that they would have been influenced by a larger strain field and thus affected by the surface plastic deformation at deeper depths compared to the smaller nanohardness indents. For the microhardness indentation, the average diagonal dimension d of the

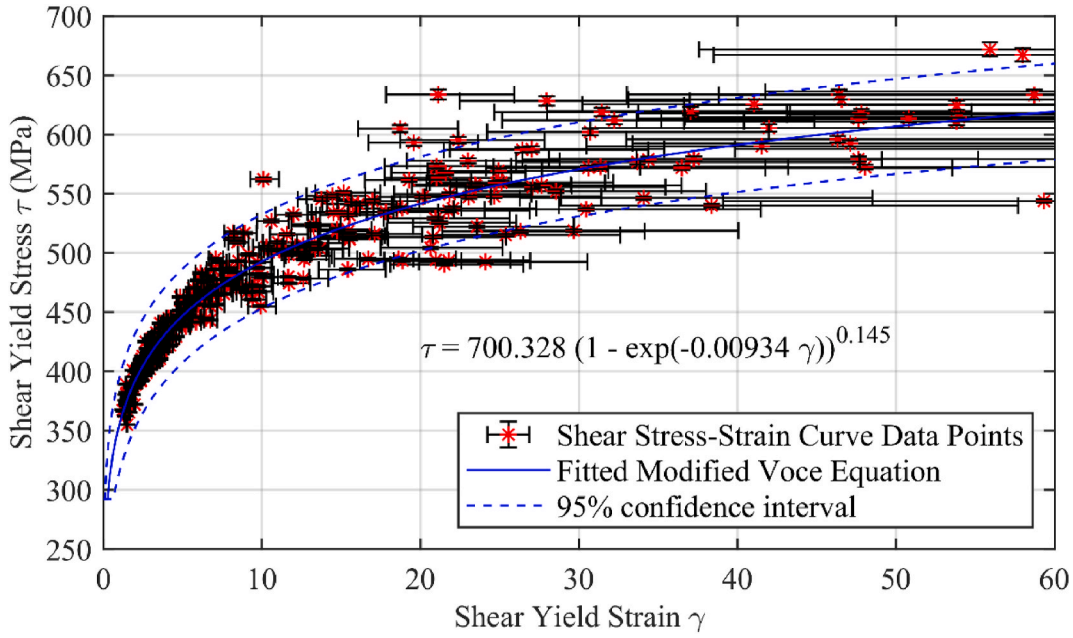

Fig. 11. Shear stress-strain curve relationship derived from R260 twin-disc sample tested up to 70,000 contact cycles for 1500 MPa, dry contact conditions.

Table 4
Shear Stress-strain Modified Voce equation coefficients determined for R260 (1500 MPa, 1200 MPa, 900 MPa, 600 MPa), HP335 (1500 MPa), and R350HT (1500 MPa).

Condition	Rail Steel Grade	Maximum Contact Pressure (MPa)	Modified Voce Equation Coefficient		
			m	n	p
1	R260	1500	700.328	0.009	0.145
2	HP335	1500	726.369	0.045	0.164
3	R350HT	1500	763.459	0.048	0.168
4	R260	1200	778.490	0.003	0.143
5	R260	900	657.127	0.018	0.176
6	R260	600	735.547	0.016	0.216

largest indents was about 20 μm and so based on half the British Standard separation requirements of *3d* between indents [13], the expected radius of the indent strain field would be approximately 30 μm (*1.5d*). A comparison of the percentage work hardening against depth relationships derived for the twin-disc samples tested up to 70,000 contact cycles for all six conditions, as presented in Fig. 9. The percentage work hardening relationship shows that all the R260 samples achieved roughly similar percentage work hardening increases in the range of 260–275% at the running surface. The HP335 and R350HT steels displayed roughly identical percentage work hardening increases to each other of about 210–225% at the specimens running surface.

4.3. Shear strain results

Fig. 10a-b shows the shear strain against depth results derived from measuring the angle of the deformed microstructure observed in the etched metallurgical samples. The results showed that the calculated shear strains increased asymptotically with the decreasing depth below the running surface. The spread of the shear strain data also increases with decreasing depth due in part to the increased error associated with converting the angles of the deformed microstructure into shear strain with Equation (5) as the angle approached 90°. In addition, there was also an observable increase in the amount of variation in the deformed microstructure angles at shallower depths.

4.4. Shear stress-strain curve relationship results

The average substrate microhardness results collected under a 10 kg indentation load for the three rail steels investigated are tabulated in Table 3. After using the relationship presented in Fig. 3 and Tresca's yield criterion, Equation (4), the initial shear yield strength for the three rail steel grades, R260, HP335, and R350HT was estimated to be 292 MPa, 374 MPa, 390 MPa, respectively.

By converting the percentage work hardening curves to shear stress using Equation (3) and combining the relationships with the shear strain against depth data, the shear stress-strain curve was derived, as shown in Fig. 11. The coefficients of the modified Voce equations fitted to the shear stress-strain curve relationship data points for the six conditions are summarised in Table 4. A comparison of the shear stress-strain curve relationships derived for the six conditions investigated are presented in Fig. 12a-b. In Fig. 12a comparing the shear stress-strain curve results obtained for the three different rail steels a clear ranking can be established between the three materials. The order in terms of the highest shear yield stress achieved was R350HT, HP335, and then R260. Comparison of the shear stress-strain curve relationship results for R260 tested at 600–1500 MPa contact pressure and dry contact conditions is shown in Fig. 12b. The results show that the shear stress-strain curve relationships are very close to one another across the contact pressures tested, showing near independence from the contact pressure, particularly at lower shear strains for which the data are least affected by uncertainties in strain measurement very close to the running surface.

5. Discussion

The hardness results presented emphasise the importance of understanding asperity driven plastic deformation near the running surface. The influence of asperity-contact driven plastic damage could be observed in the microhardness results presented in Fig. 6b. At the highest contact pressures subsurface hardening is significantly influenced by the changes in contact pressure. At the lower contact pressures explored, however, subsurface hardening becomes less influenced by bulk contact pressure. This is thought to be because for both 600 MPa and 900 MPa cases the bulk orthogonal shear stress is below the material shear yield strength, whereas localised asperity contact pressures are typically in the order of the materials hardness [28]. The effect of

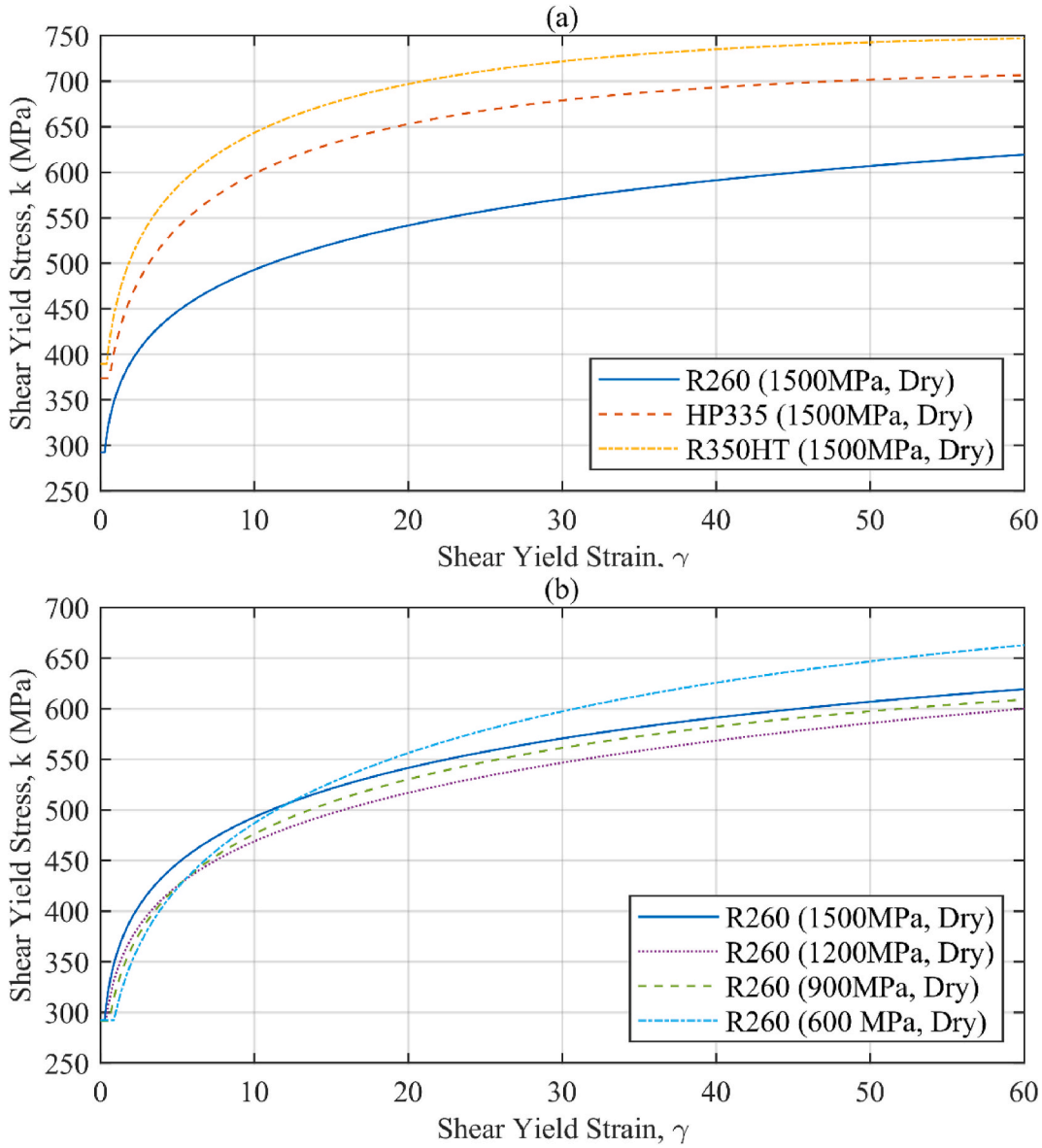

Fig. 12. Comparison of the shear stress-strain curve relationships for a) R260 (1500 MPa), HP335 (1500 MPa), and R350HT (1500 MPa); and b) R260 (1500 MPa, 1200 MPa, 900 MPa, 600 MPa) under dry contact conditions. Values at high shear strain (over ~25) are particularly susceptible to uncertainty in the underlying data as shown in Fig. 11.

asperity-contact driven plastic damage was also observed in the nano-hardness data, shown in Fig. 7, with the noticeable increase in the hardness-depth plot gradient within 50–100 μm of the running surface. The influence of asperity contact driven plastic damage can also help explain why reduced wear was observed for the 900 MPa and 600 MPa contact pressure R260 experiments shown in Fig. 5b. This is because for the 1500 MPa and 1200 MPa R260 tests, the plastic deformation for these conditions would be observed to be a combination of asperity and bulk plasticity. Tyfour et al. [9] showed that the wear observed for this type of plastic damage accumulation increases initially due to the build-up of bulk subsurface strain. A steady-state wear rate is achieved when the subsurface shear strain against depth profile also becomes steady state. For the 900 MPa and 600 MPa contact pressure experiment, a predominantly asperity contact pressure driven plastic deformation would be observed. Under these conditions the orthogonal shear stresses localised at the surface for asperity contacts are significantly higher compared to the stress deeper down. These significantly higher shear stress will then cause the surface material to accumulate shear strain and reach a steady-state strain against depth profile quicker. Thus, a steady-state wear rate should be achieved for predominantly asperity contact driven plastic deformation sooner than for bulk plasticity.

An interesting finding from the nanohardness results, shown in Fig. 7, was the similar nanohardness values of about 12 GPa at the surface of the twin-disc samples for all six conditions investigated. This is despite the three rail steels tested having different initial metallurgy and baseline hardness, and the different contact pressures investigated. This could point to the influence of surface roughness leading to very high asperity contact pressures which will cause flow as they exceed the yield stress in a particular material. There is the potential for feedback between asperity pressures, yield point and surface modification resulting in similar amounts of plastic shear strain at the running surface across the tests. An alternative explanation is that the results could show a limiting hardness value that the pearlitic microstructure of rail steels can achieve under combined compression-shear loading conditions before failing.

The comparison of the shear stress-strain curve relationships for R260, HP335, and R350HT in Fig. 12a demonstrates the different material behaviour of these three rail steel metallurgies subject to the same

conditions. The results showed that the ranking of the rail steel grades in term of the highest shear yield strength achieved is R350HT, HP335, and R260. However, this order is not carried over to the wear rate results with HP335 rail steel performing better than R350HT in term of the lowest wear rate observed for the same contact conditions. The difference in ranking indicates that the shear stress-strain curve and the shear yield point by themselves are not enough to determine which rail steels will have the lower wear rate. The shear strain that the material can sustain before failure and the rate of shear strain accumulation in response to each load cycle are vital additional pieces of information to determine behaviour. For example, the highest shear strains in Fig. 12 may not be achieved uniformly throughout the deformed material.

The shear stress-strain curve relationships obtained for R260 at different contact pressures (1500 MPa, 1200 MPa, 900 MPa, 600 MPa) are compared in Fig. 12b. The results showed that the shear stress-strain curve relationship for R260 was roughly similar across the four different contact pressures tested. This shows that within this range of pressures the shear stress-strain relationship derived from twin-disc samples is near to independent of the contact pressures at which the data is collected. The shear stress-strain curve relationship obtained can, therefore, be classed as 'material property' data rather than 'system behaviour' data. The implication of this is that the shear stress-strain curve relationship derived from twin-disc samples tested at 1500 MPa, is suitable for describing the material behaviour of rail steel when subjected to different contact pressure ranging from the 600–1500 MPa range tested. This is helpful for simulation models, such as the 'Layer' and 'Brick' model, as separate shear stress-strain relationships for different contact pressures are not needed.

6. Conclusions

The rail steel shear stress-strain curve relationship has been derived from characterising the plastic deformation observed in twin-disc samples for a range of different rail steel metallurgies and contact conditions. From this work the following conclusions can be made:

- HP335 was seen to be the better performer in the wear tests showing a distinctly lower overall wear rate compared to R350HT and R260.
- The ranking of the shear stress-strain curve relationships for R260, HP335, R350HT rail steel subject to 1500 MPa, dry contact conditions can be clearly established. The order in terms of highest shear yield stress achieved was R350HT, HP335, and then R260. This indicates that the shear stress-strain curve relationships alone are insufficient to fully capture wear behaviour in a laboratory environment.
- Comparison of the shear stress-strain curve relationships obtained for R260 rail steel subject to different contact pressures (1500 MPa, 1200 MPa, 900 MPa, 600 MPa) generated near identical relationships. This indicates that (at least within this range of working pressures) the shear stress-strain curves obtained can be classed as 'material property' data rather than 'machine behavioural' data that is only applicable for the same contact conditions the data was collected with.

Declaration of competing interest

The authors declare that they have no known competing financial interests or personal relationships that could have appeared to influence the work reported in this paper.

Data availability

Data will be made available on request.

Acknowledgements

The authors would like to acknowledge the EPSRC (Engineering and Physical Sciences Research Council) through the Advanced Metallic Systems CDT (EPSRC grant ref. EP/L016273/1) and British Steel Ltd. for providing the funding for this research. The authors would also like to thank British Steel Ltd. for providing the rail steel and Wabtec Rail Ltd. for providing the wheel steel used to manufacture the twin-disc samples tested in this work.

References

[1] N.P. Suh, The delamination theory of wear, Wear 25 (1) (Jul. 1973) 111–124, https://doi.org/10.1016/0043-1648(73)90125-7.
[2] Network Rail, Network Rail Infrastructure Limited: Regulatory Financial Statements 2021/22, 2022 [Online]. Available: https://www.networkrail.co.uk/who-we-are/publications-and-resources/financial/.
[3] A. Kapoor, K.L. Johnson, Plastic ratchetting as a mechanism of metallic wear, Proc. R. Soc. London. Ser. A Math. Phys. Sci. 445 (1924) (May 1994) 367–384, https://doi.org/10.1098/rspa.1994.0066.
[4] A. Kapoor, J.H. Beynon, D.I. Fletcher, M. Loo-Morrey, Computer simulation of strain accumulation and hardening for pearlitic rail steel undergoing repeated contact, J. Strain Anal. Eng. Des. 39 (4) (May 2004) 383–396, https://doi.org/10.1243/0309324041223935.
[5] F.J. Franklin, I. Widiyarta, A. Kapoor, Computer simulation of wear and rolling contact fatigue, Wear 251 (1–12) (Oct. 2001) 949–955, https://doi.org/10.1016/S0043-1648(01)00732-3.
[6] W.R. Tyfour, J.H. Beynon, A. Kapoor, Deterioration of rolling contact fatigue life of pearlitic rail steel due to dry-wet rolling-sliding line contact, Wear 197 (1–2) (Sep. 1996) 255–265, https://doi.org/10.1016/0043-1648(96)06978-5.
[7] K. Tomlinson, D.I. Fletcher, R. Lewis, Measuring material plastic response to cyclic loading in modern rail steels from a minimal number of twin-disc tests, Proc. Inst. Mech. Eng. - Part F J. Rail Rapid Transit 235 (10) (Feb. 2021) 1203–1213, https://doi.org/10.1177/0954409721993615.
[8] F.A.M. Alwahdi, A. Kapoor, F.J. Franklin, Subsurface microstructural analysis and mechanical properties of pearlitic rail steels in service, Wear 302 (1–2) (Apr. 2013) 1453–1460, https://doi.org/10.1016/j.wear.2012.12.058.
[9] W.R. Tyfour, J.H. Beynon, A. Kapoor, The steady state wear behaviour of pearlitic rail steel under dry rolling-sliding contact conditions, Wear 180 (1–2) (Jan. 1995) 79–89, https://doi.org/10.1016/0043-1648(94)06533-0.
[10] A. Wilby, J. Corteen, R. Lewis, D.I. Fletcher, In-Situ Optical Monitoring of Very Early-Stage Rail Wear and Rolling Contact Fatigue Crack Initiation in Laboratory Testing, 2022.
[11] Phoenix Tribology Ltd, TE 72 two roller machine, http://www.phoenix-tribology.com/at2/leaflet/te72, 2017.
[12] D.I. Fletcher, J.H. Beynon, Development of a machine for closely controlled rolling contact fatigue and wear testing, J. Test. Eval. 28 (4) (Jul. 2000) 267–275, https://doi.org/10.1520/JTE12104J.
[13] British Standards. Metallic Materials. Vickers Hardness Test. Test Method, 2018. BS EN ISO 6507-1:2018.
[14] W.C. Oliver, G.M. Pharr, An improved technique for determining hardness and elastic modulus using load and displacement sensing indentation experiments, J. Mater. Res. 7 (6) (1992) 1564–1583, https://doi.org/10.1557/JMR.1992.1564.
[15] N.A. Fleck, G.M. Muller, M.F. Ashby, J.W. Hutchinson, Strain gradient plasticity: theory and experiment, Acta Metall. Mater. 42 (2) (Feb. 1994) 475–487, https://doi.org/10.1016/0956-7151(94)90502-9.
[16] D.I. Fletcher, J.H. Beynon, The influence of lubricant type on rolling contact fatigue of pearlitic rail steel, in: D. Dowson, M. Priest, C.M. Taylor, P. Ehret, T.H. C. Childs, G. Dalmaz, Y. Berthier, L. Flamand, J.M. Georges, A.A. Lubrecht (Eds.), Lubrication at the Frontier, 36, Elsevier, 1999, pp. 299–310.
[17] D. Nikas, X. Zhang, J. Ahlström, Evaluation of local strength via microstructural quantification in a pearlitic rail steel deformed by simultaneous compression and torsion, Mater. Sci. Eng., A 737 (2018) 341–347, https://doi.org/10.1016/j.msea.2018.09.067.
[18] K.A. Meyer, M. Ekh, J. Ahlström, Modeling of kinematic hardening at large biaxial deformations in pearlitic rail steel, Int. J. Solid Struct. 130 (131) (2018) 122–132, https://doi.org/10.1016/j.ijsolstr.2017.10.007.
[19] O. Yazici, S. Yilmaz, S. Yildirim, Microstructural and mechanical properties examination of high-power diode laser-treated R260 Grade rail steels under different processing temperatures, Metall. Mater. Trans. A 50 (2) (2019) 1061–1075, https://doi.org/10.1007/s11661-018-5041-1.
[20] O. Hajizad, A. Kumar, Z. Li, R.H. Petrov, J. Sietsma, R. Dollevoet, Influence of microstructure on mechanical properties of bainitic steels in railway applications, Metals 9 (7) (2019), https://doi.org/10.3390/met9070778.
[21] A. Kumar, et al., Design of high-strength and damage-resistant carbide-free fine bainitic steels for railway crossing applications, Mater. Sci. Eng., A 759 (Jun. 2019) 210–223, https://doi.org/10.1016/j.msea.2019.05.043.
[22] A.C. Athukorala, D. V De Pellegrin, K.I. Kourousis, Characterisation of head-hardened rail steel in terms of cyclic plasticity response and microstructure for

improved material modelling, Wear 366 (367) (Nov. 2016) 416–424, https://doi.org/10.1016/j.wear.2016.03.024.
[23] S. Maya-Johnson, A.J. Ramirez, A. Toro, Fatigue crack growth rate of two pearlitic rail steels, Eng. Fract. Mech. 138 (Apr. 2015) 63–72, https://doi.org/10.1016/j.engfracmech.2015.03.023.
[24] W. Hui, Z. Xu, Y. Zhang, X. Zhao, C. Shao, Y. Weng, Hydrogen embrittlement behavior of high strength rail steels: a comparison between pearlitic and bainitic microstructures, Mater. Sci. Eng., A 704 (Sep. 2017) 199–206, https://doi.org/10.1016/j.msea.2017.08.022.
[25] H. Su, et al., Ratcheting behaviour of flash butt welds in heat-treated hypereutectoid steel rails under uniaxial and biaxial cyclic loadings, Int. J. Mech. Sci. 176 (Jun. 2020) 105539, https://doi.org/10.1016/j.ijmecsci.2020.105539.
[26] R.R. Porcaro, G.L. Faria, L.B. Godefroid, G.R. Apolonio, L.C. Cândido, E.S. Pinto, Microstructure and mechanical properties of a flash butt welded pearlitic rail, J. Mater. Process. Technol. 270 (Aug. 2019) 20–27, https://doi.org/10.1016/j.jmatprotec.2019.02.013.
[27] British Steel, R260 and HP335 Tensile and Hardness Test Results, 2021.
[28] J.F. Archard, T.E. Allibone, Elastic deformation and the laws of friction, Proc. R. Soc. London. Ser. A. Math. Phys. Sci. 243 (1233) (Jan. 1997) 190–205, https://doi.org/10.1098/rspa.1957.0214.
[29] Railway Applications - Track - Rail - Part 1: Vignole Railway Rails 46 Kg/m and above, 2011. BS EN13674-1.
[30] Railway Rolling Stock Materials. Specification for Monobloc Wheels for Traction and Trailing Stock, 1992. BS 5892-3.
[31] British Steel, Steel Compositions and Properties," *Rail Product Guide*, 2017. https://britishsteel.co.uk/media/40810/steel-grade-dimensions-and-properties.pdf.